More Frequent Extreme Precipitation on the Asian Monsoon Fringes Driven by Evolving Extratropical Planetary-Scale Circulations

Zhenyu You[1*], Yi Deng[1], Yi Ming[2], and Jaeyoung Hwang[1]

1. School of Earth and Atmospheric Sciences, Georgia Institute of Technology, Atlanta, GA, USA
2. Schiller Institute for Integrated Science and Society, Department of Earth and Environmental Sciences, Boston College, Chestnut Hill, MA, USA

**Corresponding author*: Zhenyu You (zhenyu.you@bc.edu)

Present address: Schiller Institute for Integrated Science and Society, Boston College, Chestnut Hill, MA, USA.

Preprint Status: This is a non-peer reviewed preprint submitted to EarthArXiv.

Journal Submission: This manuscript has been submitted to *Geophysical Research Letters* for peer review.

Abstract

In recent decades, the fringes of the Asian summer monsoon, such as Pakistan and Northeast China, have become hotspots of extreme precipitation. Although such increases are often linked to thermodynamic changes in a warming climate, the dynamical drivers behind these trends, particularly the systematic role of extratropical circulations, remain poorly understood. This study identifies the large-scale atmospheric circulation patterns responsible for intense summertime rainfall in Northeast China and Pakistan. Clustering analysis reveals that the recent increase in intense precipitation is driven by a distinct shift in the preferred Rossby wave pathways over Eurasia. Dynamical analysis with an idealized model indicates that this shift is driven by an evolving upper-tropospheric mean flow which modifies atmospheric instability and wave propagation. These results highlight the need to understand the origins of extratropical background flow changes to improve projections of regional precipitation in a changing climate.

Plain Language Summary:

In recent years, regions on the fringes of the Asian summer monsoon, such as Pakistan and Northeast China, have suffered from increasingly frequent and severe floods. While a warmer climate contributes to this by allowing the air to hold more moisture, we find that changes in midlatitude atmospheric circulations play a critical role. We identify three distinct pathways that atmospheric waves follow across Eurasia to reach these regions. Critically, a recent shift in the summer jet stream has effectively guided these waves along a preferred "central" path, which impacts both Pakistan and Northeast China. Idealized modeling further confirms that these changes in the background circulations have made the atmosphere more favorable for this specific wave path to develop.

1 Introduction

The Asian summer monsoon, a major component of the global climate system, brings heavy summer rainfall across southern and eastern Eurasia each year. It consists of the South Asian Summer Monsoon (SASM) and the East Asian Summer Monsoon (EASM). The SASM brings most of the annual precipitation over South Asia between June and September and is characterized by distinct monsoonal dynamics (B. Wang, 2006; Webster et al., 1998). By contrast, the EASM exhibits more complex spatiotemporal structures. It extends from subtropical to midlatitude regions, with elongated rain belts (the Meiyu/Jangma/Baiu front) stretching thousands of kilometers (Ding et al., 2020; Hu et al., 2021).

In recent decades, regions at the fringes of the Asian summer monsoon such as Pakistan and Northeast China have become hotspots of hydrological extremes (Nanditha et al., 2023; Tang et al., 2023). Northeast China lies near the northern extent of the EASM where summer rainfall accounts for up to two-thirds of the annual total (Chen et al., 2015). Since the 1990s, anomalous summer precipitation events have become more frequent, leading to major agricultural and economic losses (T. Gao et al., 2017; Sun & Ao, 2013; Yu & Ma, 2022). Pakistan lies at the northwestern edge of the SASM, where monsoonal moisture lifted over the Himalayan terrain produces intense rainfall and floods (Khan & Hasan, 2019). The 2022 Pakistan flood, driven by record-breaking rainfall from mid-June through August, led to a death toll surpassing the toll of the famous 2010 flood (Nanditha et al., 2023).

Precipitation in the Asian monsoon fringes is largely controlled by the spatiotemporal variability of monsoonal circulations. In Northeast China, the enhanced moisture transport from low-level southerly wind anomalies in EASM serve as a strong indicator of intense rainfall (L. Sun et al., 2007, 2017). Similarly, much of Pakistan's precipitation variability arises from spatiotemporal fluctuations of the SASM circulation, along with varying activities of synoptic systems such as monsoon lows originating near the Bay of Bengal (Houze et al., 2011; Hurley & Boos, 2015; Y. You & Ting, 2021). Changes in thermodynamic processes, including the enhanced moisture-holding capacity of the atmosphere under a warming climate, have also been argued to be partly responsible for the amplified extreme rainfall in Pakistan in recent decades (Ullah et al., 2023; Y. You et al., 2024).

Beyond direct and indirect influences from monsoonal circulations, precipitation in monsoon fringes is also affected by extratropical dynamics. The Summer North Atlantic Oscillation (SNAO) can induce meridional dipole patterns in rainfall over central and northern East Asia by modulating stationary wave activity across Eurasia, leaving a clear footprint on Northeast China precipitation (Shen et al., 2011; Sun & Wang, 2012; Z. Wang et al., 2018). Likewise, intrusions of upper-level troughs from higher latitudes into northern Pakistan have also contributed to regional extreme rainfall (Dengri & Yamada, 2024; Lau & Kim 2012; Trenberth & Fasullo, 2012). While these studies highlight important mechanisms from higher latitudes, the current body of literature remains heavily focused on monsoon-related dynamic and thermodynamic processes. In contrast, systematic assessments of the extratropical circulation regimes that trigger extreme rainfall remain limited. The variability and trends of these circulation patterns, along with the processes driving their initiation and development under varying climate conditions, are not well understood.

To address this gap, this study systematically identifies the large-scale extratropical circulation patterns responsible for intense June-August (JJA) precipitation in Northeast China and Pakistan. To explain trends in the frequency of occurrence of the identified wave patterns, we examine changes in the JJA mean flow and apply optimal mode analysis using an idealized barotropic model linearized around the JJA background flow in the early and late periods of the past four decades. Finally, we assess the consistency between shifts in optimal mode characteristics and observed trends in the identified wave patterns to reveal the dynamical origins of long-term trends in intense rainfall over monsoon fringes.

2 Materials and Methods

2.1 Clustering of Large-scale Circulation Patterns Triggering Intense Precipitation

To systematically evaluate the large-scale forcing mechanisms of intense precipitation, we perform hierarchical clustering analysis using Ward's method (Ward, 1963; Z. You et al., 2024) on large-scale circulation patterns associated with high-precipitation days over Northeast China (40°-50°N, 120°-130°E). Precipitation percentiles are computed using a ±20-day window centered on each calendar day within JJA. Days with precipitation exceeding the 50th percentile are identified as days of intense precipitation. For these selected days, 250 hPa geopotential height anomalies from day −4 to day 0 are extracted as the basis for clustering. The spatial domain of classification spans 30°-70°N and 0°-140°E. The purpose of choosing this broad spatiotemporal domain is to capture the full upstream evolution of disturbances (Z. You & Deng, 2022) influencing Northeast China. Cases with overlapping days are excluded prior to clustering.

2.2 Linear Barotropic Model

In this study, we apply a quasi-geostrophic barotropic model at the 250 hPa pressure level on a midlatitude channel domain spanning 20°-80°N (Holton & Hakim, 2013; Mak, 2011). Linear damping on relative vorticity is applied to mimic the spin-down effect associated with the presence of a planetary boundary layer (Holton & Hakim, 2013). A hyperdiffusion term is added for scale selection to damp grid- and subgrid-scale waves (Sardeshmukh & Hoskins, 1988; Simmons et al., 1983). The model is linearized around a background flow. In this study, two background flows are used: the JJA mean geopotential height at 250 hPa averaged over 1982-2002 and 2003-2023. To test robustness, we select three combinations of linear damping parameters and three hyperdiffusion parameters. Details of the model setup are provided in supporting Text S1.

2.3 Optimal Mode (Nonmodal Instability) Analysis

After constructing the dynamical model with boundary conditions and finite differencing, we apply optimal mode (nonmodal instability) analysis (Z. You & Deng, 2025; Zhao et al., 2018, 2020; Zhao & Deng, 2020). This analysis identifies the initial disturbances that amplify most rapidly (in terms as wave amplitude) over a specified time interval on a prescribed background flow. Local optimization over the domain of clustering analysis in Section 2.1 is adopted by applying heavier weights in the wave amplitude over the target domain. The optimal disturbances are constructed as linear combinations of all intrinsic normal modes and are obtained through an eigenvalue problem, which yields the structures of the optimal modes for the chosen time interval and their amplification factors. Detailed procedures for obtaining the optimal modes are provided in supporting Text S2.

2.4 Data

The observational precipitation comes from the Climate Prediction Center (CPC) global unified gauge-based analysis of daily precipitation data with spatial resolution of 0.5°×0.5° (Xie et al., 2007). The atmospheric variables come from the fifth generation of ECMWF reanalysis dataset (ERA5) with spatial resolution of 0.25°×0.25° (Hersbach et al., 2020).

3 Results

3.1 Climatology and Decadal Trends of JJA Precipitation

Figure 1 illustrates the spatial distribution and long-term trends of JJA precipitation across the Eurasian continent. During JJA, the heaviest precipitation across East and Central Asia occurs over the monsoon regions (Figure 1a). To highlight the relative magnitude of precipitation changes, Figure 1b shows normalized local precipitation trends by dividing them by the corresponding climatological means as shown in Figure 1a. A significant wetting trend extends across much of Eurasia, with the strongest increases near the monsoon regions and their fringes, including Pakistan, Bangladesh, Myanmar, and eastern China.

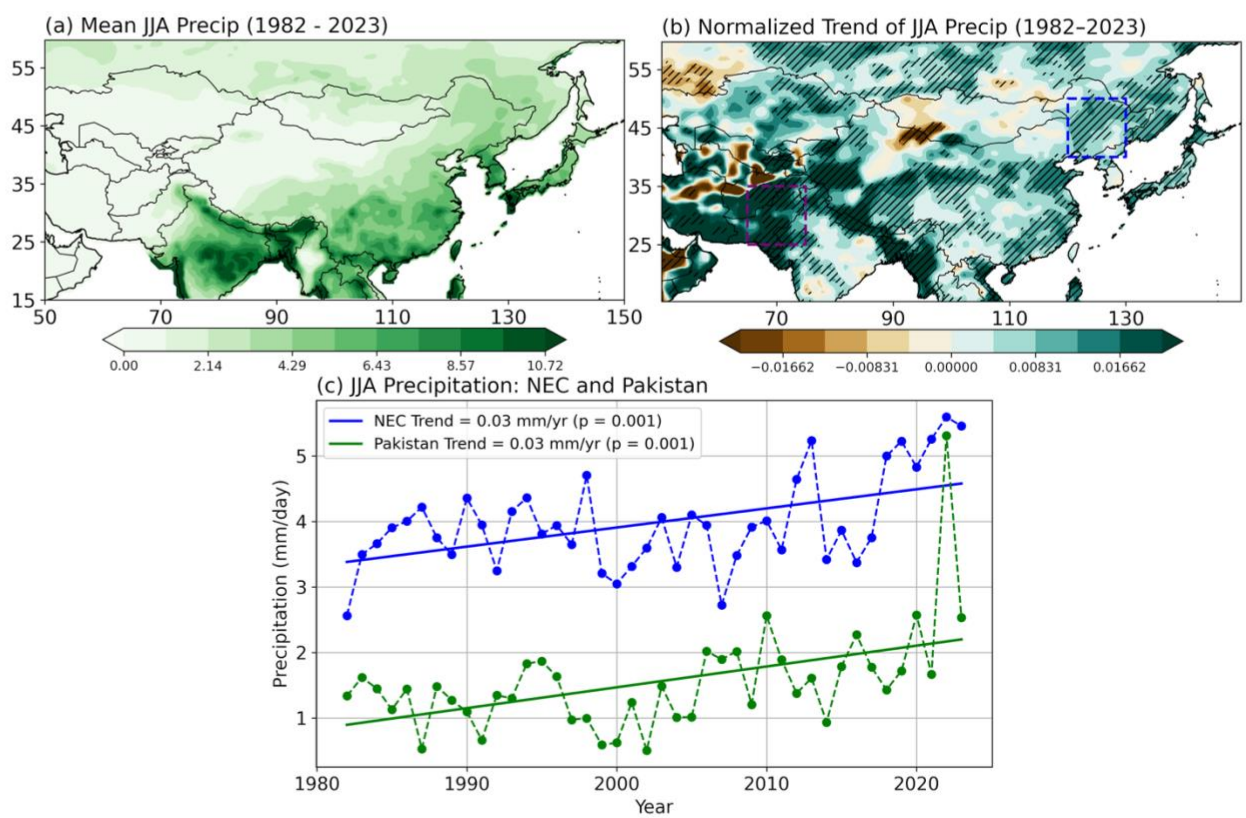

Figure 1. (a) Climatology of JJA (June-August) mean precipitation (mm/day) over East and Central Asia during 1982–2023. (b) Interannual trend in JJA mean precipitation (mm/day/year) over the same period normalized by the climatology in (a). (c) Time series and trend lines, for JJA mean precipitation averaged over Northeast China (40°-50°N, 120°-130°E; blue lines) and the Pakistan region (25°-35°N, 65°-75°E; green lines).

In the two focus regions of this study, i.e., Northeast China (blue box in Figure 1b) and Pakistan (purple box in Figure 1b), Figure 1c further demonstrates that both Northeast China and Pakistan have experienced comparable upward trends, despite receiving less rainfall on average than the core monsoon regions of East and South Asia. The absolute magnitudes of the trends are similar in both regions (~0.03 mm $day^{-1}year^{-1}$), although the relative increase is smaller in Northeast China due to its larger climatological mean. Notably, 2010 and 2022 stand out as exceptionally wet years in Pakistan, and 2013 and 2022 in Northeast China. The consistent upward trends across both northern and western monsoon fringes emphasize the need to examine the circulation anomalies responsible for this intensification.

3.2 Large-Scale Forcing Patterns Triggering Intense Precipitation

The hierarchical clustering on the large-scale circulation patterns preceding extreme events (in Section 2.1) reveals three dominant circulation patterns (clusters) associated with intense precipitation in Northeast China. All three composite forcing patterns feature quasi-stationary Rossby waves with low phase speeds and evident downstream energy dispersion (Figure 2). Cluster 1 features an intense low-pressure anomaly over Scandinavia and a pronounced ridge over northern Siberia. The circulation pattern near Northeast Asia resembles the "dipole pattern" (anomalies over northern Siberia and East Asia) linked to the Summer North Atlantic Oscillation (SNAO) (Sun & Wang, 2012). Cluster 2 is characterized by a strong high-pressure anomaly over eastern Europe, with downstream energy dispersing toward Northeast China by day 0. Cluster 3 features a wave train extending from northern Europe into central Asia, with weaker energy dispersion into Northeast China. Clusters 1, 2, and 3 account for 39%, 31%, and 30% of intense precipitation events in Northeast China, respectively.

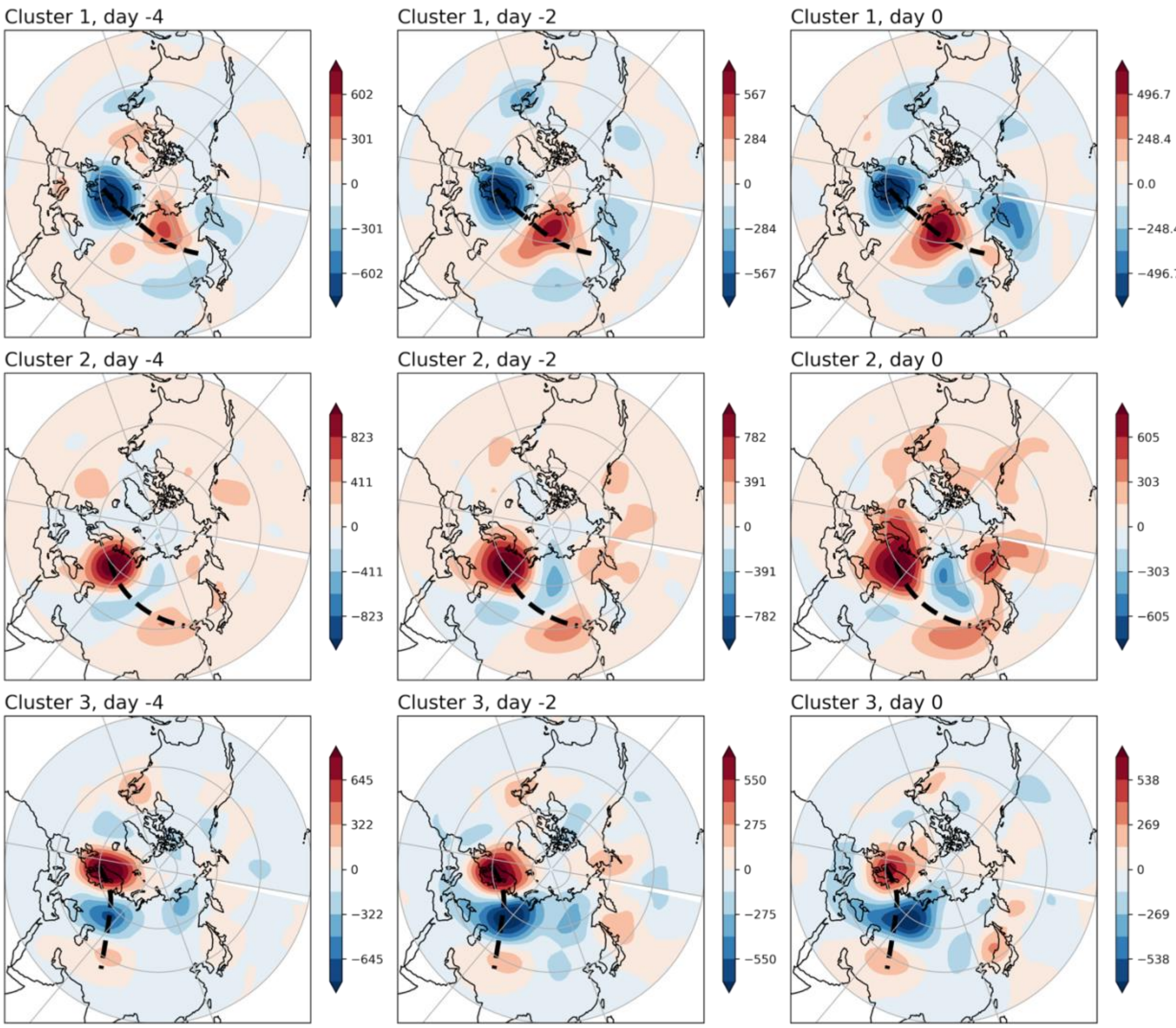

Figure 2. Composite anomalies of 250 hPa geopotential (shading; m^2/s^2) associated with each cluster from day −4 to day 0. Columns represent different lead times (−4, −2, and 0 days), and rows correspond to individual clusters. Black dashed lines indicate approximate pathways of disturbance propagation within each cluster.

The three clusters exhibit distinct circulation patterns and particularly distinct pathways of wave energy dispersion, illustrated by black dashed lines in Figure 2. Cluster 1 follows a zonal pathway stretching from Scandinavia across Siberia into Northeast Asia. Cluster 2 propagates across Mongolia into eastern China, indicating a “central” pathway, while Cluster 3, characterized by an equatorward pathway, tracks along a great-circle route moving across central Asia. As shown later (Figure 4), these pathways are closely linked to changes in the cluster occurrence frequency between the early (1982-2002) and recent (2003-2023) period.

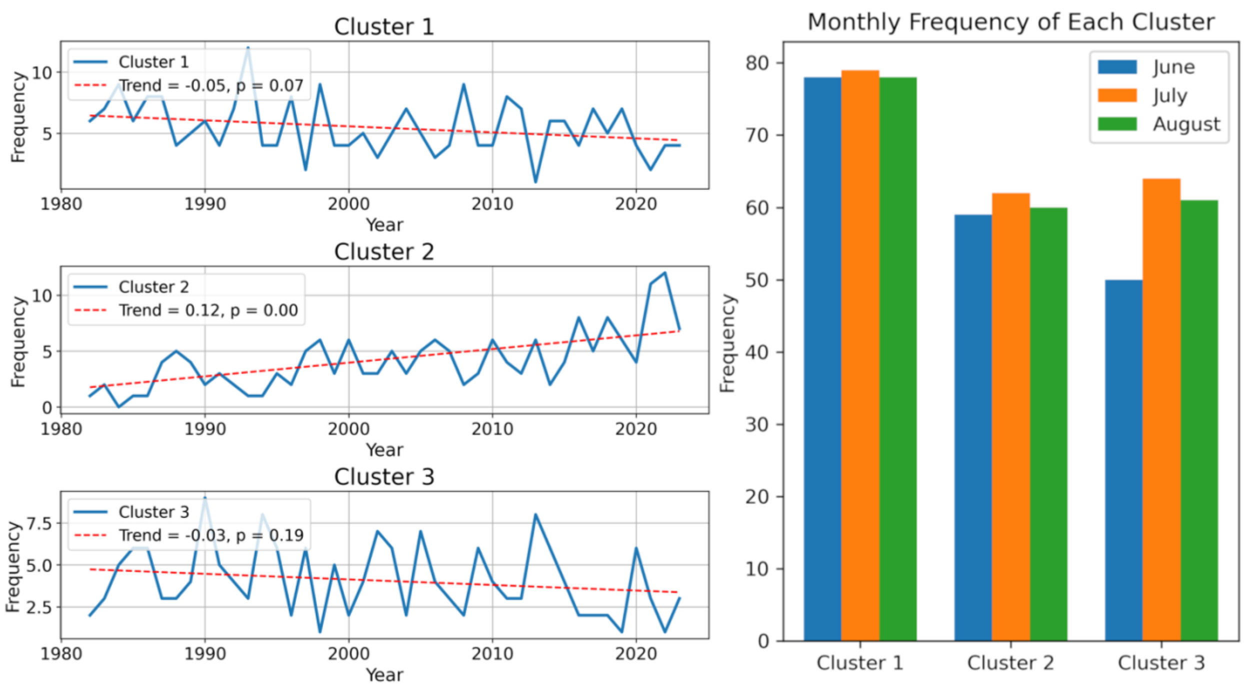

Figure 3. (Left) Interannual time series and linear trends in the JJA frequency of each cluster from 1982 to 2023. Each panel shows the annual frequency of clusters with the linear trend line (red dashed). (Right) Monthly frequency of each cluster during June, July, and August.

Clusters 1 and 3 occur with similar frequency across June, July, and August, while Cluster 2 is more common in July and August (Figure 3, right). In terms of interannual frequency, only Cluster 2 exhibits a statistically significant positive trend over the past 40 years (Figure 3, left). Interestingly, Cluster 2 frequently leads to intense precipitation in Pakistan in addition to Northeast China. For instance, during July-August 2010, the persistent Pakistan flood and the Russian heat wave, were dynamically connected through an extratropical circulation pattern resembling Cluster 2 (Di Capua et al., 2021; Lau & Kim, 2012). Although many studies have analyzed the meteorological patterns associated with these events (Di Capua et al., 2021; Lau & Kim, 2012; Trenberth & Fasullo, 2012), efforts to trace the origins of the relevant large-scale disturbances remain inconclusive. The robust upward trend in the Cluster 2 occurrence motivates further investigation, which forms the focus of the remainder of this study.

3.3 Changes in Summer Mean Flow and Rossby Waveguides

To explain the observed changes in cluster occurrence frequency, we first examine differences in the background (summer mean) flow between the later period (2003-2023) and the earlier period (1982-2002) (Figure 4). The background shifts match with the observed trends in the extratropical Rossby wave pathway in Figure 3. The shift and extension of the North Atlantic jet in the later period (Figure 4b) supports greater downstream wave propagation, consistent with the increasing frequency of Cluster 2 and the decreasing frequencies of Clusters 1 and 3 over the past four decades (Figure 3). The intensified Asian jet and its extension into Northeast China (Figure 4b) also align with the rising trend in intense precipitation in that region.

To connect mean flow changes with Rossby wave propagation, we calculate the stationary wavenumber *Ks* following the waveguide formulation (Hoskins & Ambrizzi, 1993):

$$K_s = a\,(\frac{\beta_M}{U_M})^{1/2} \qquad (1)$$

where U_M is the mean zonal wind, a is Earth's radius, and β_M is the meridional gradient of the absolute vorticity (planetary vorticity f and relative vorticity of the background flow U_M). The full expression for β_M is:

$$\beta_M = \frac{2\Omega cos^2\varphi}{a} - \frac{cos\varphi}{a^2}\frac{\partial}{\partial\varphi}\frac{1}{cos\varphi}\frac{\partial}{\partial\varphi}(U_M cos^2\varphi) \qquad (2)$$

Stationary Rossby waves tend to refract toward large *Ks* values. Thus, local maxima in *Ks* act as "paths" guiding the propagation of quasi-stationary Rossby waves (Branstator, 2002; Branstator & Teng, 2017; Hoskins & Ambrizzi, 1993).

Changes in K_S are largely consistent with changes in the mean zonal wind (Figure 3c). The waveguide extends farther into Europe and strengthens within the Asian jet region during the recent two decades, while K_S decreases slightly on the northern and southern flanks of the high-K_S core. Shifts in K_s and mean zonal wind indicate that background summer mean flow changes favor a more active "central" pathway (Cluster 2) and less active "zonal" (Cluster 1) and "equatorward" pathway (Cluster 3) of wave propagation in recent decades.

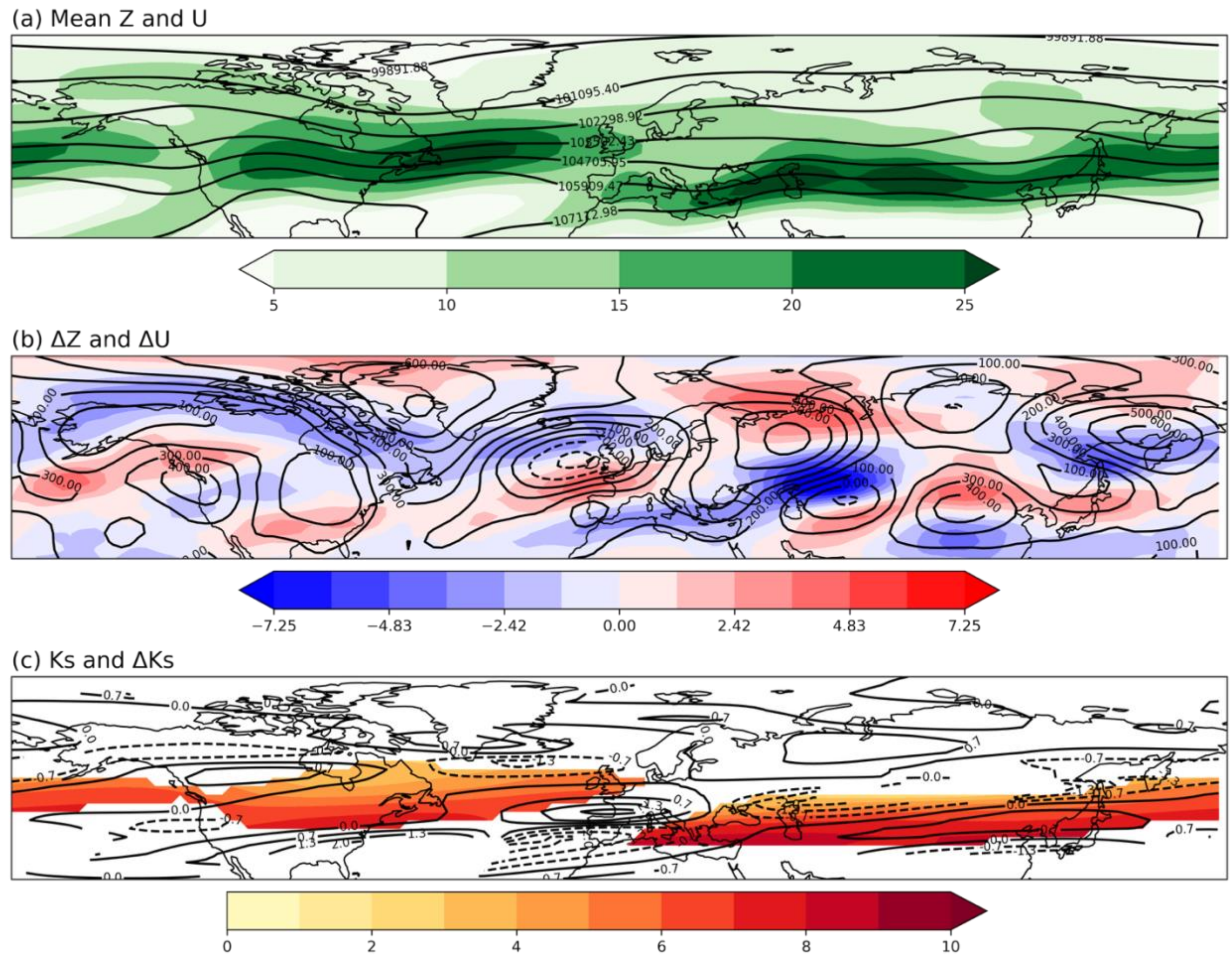

Figure 4. (a) JJA climatology of 250 hPa geopotential (contours, m^2/s^2) and zonal wind (shading, m/s) for 1982-2002. (b) Difference in 250 hPa geopotential (contours, m^2/s^2) and zonal wind (shading, m/s) between 2003–2023 and 1982–2002. (c) JJA climatology of zonal stationary wave number, shown only where the zonal-mean wind exceeds 15 m/s (color shading) and difference in zonal stationary wave number between the two periods (contours).

3.4 Optimal Modes in a Linear Barotropic Model

The mean flow and waveguide analysis provides a preliminary explanation for the observed changes in wave pathways. To further understand how changes in mean flow affect wave characteristics such as excitation and propagation, we conduct an optimal mode analysis (Section 2.3), using a barotropic model linearized around the early and late mean flows (Section 2.2). Differences in optimal mode statistics between the early and later period highlight the impact of mean flow changes on the properties of Rossby waves (optimal modes) that spontaneously grow and subsequently decay within the mean flow.

The optimal modes obtained from this highly idealized model of the upper troposphere closely resemble the cluster patterns seen in Figure 2. The upper panels of Figure 5 show the evolution of the leading optimal mode for optimization time $\tau = 10$ days, a timescale representative of quasi-stationary atmospheric disturbances such as the identified clusters. The disturbance originates over eastern North America. By day 10 (the optimization time), it evolves into a Rossby wave train extending from the North Atlantic into Eurasia with a strong high anomaly over Scandinavia. By day 20, this high anomaly persists over Scandinavia and eastern Europe, with significant downstream dispersion toward Pakistan and Northeast China. The overall wave structure over Eurasia closely matches the composite height anomalies of Cluster 2. The subsequent (2^{nd} to 5^{th}) optimal modes for $\tau = 10$ days are shown in Figure S1.

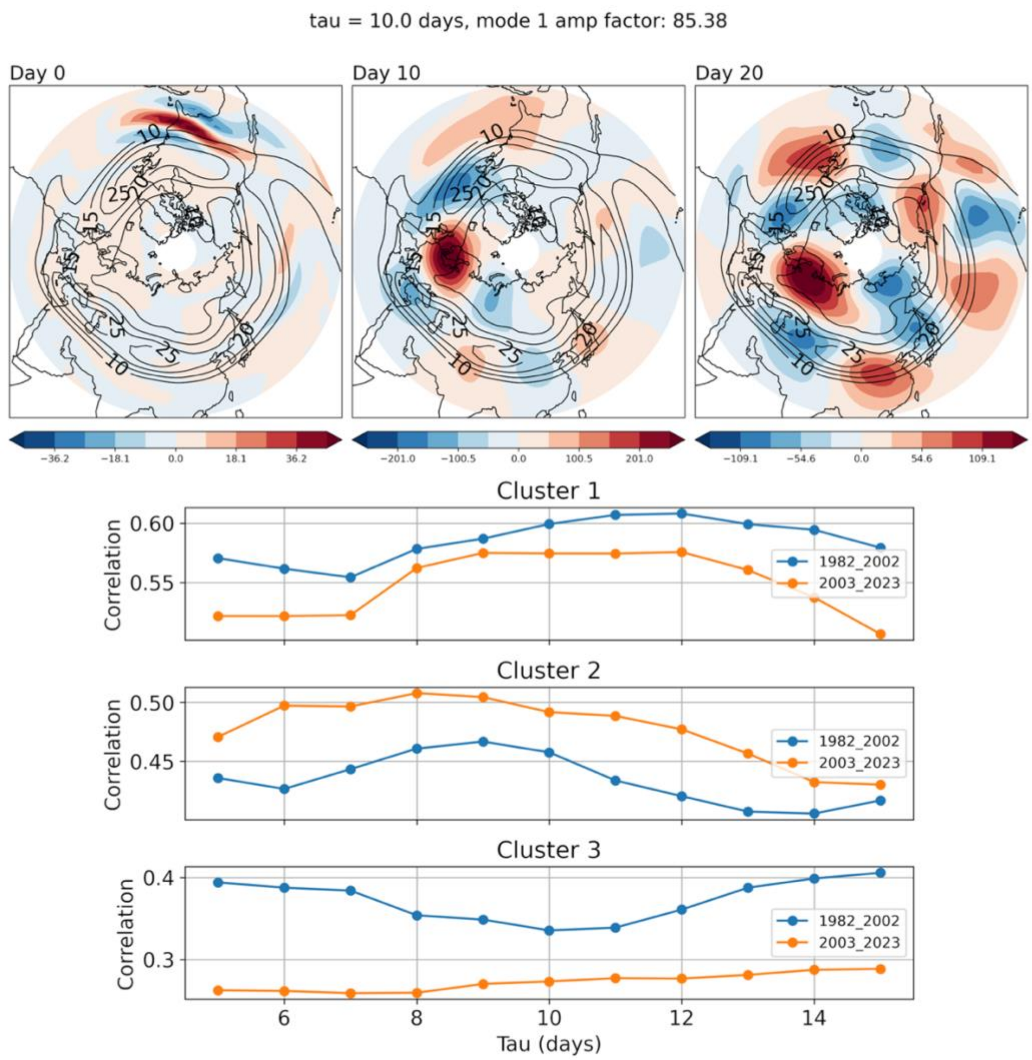

Figure 5. (Top) Spatial evolution of the first optimal mode using the mean flow of JJA 1982–2002 with τ = 10 days. Shading indicates the evolving disturbance patterns and contours show the background zonal wind (m/s). (Bottom) Weighted average of the maximum correlation between optimal modes and day 0 cluster composite patterns as a function of τ (in days), for each cluster. Results are shown for two periods: 1982–2002 (blue) and 2003–2023 (orange).

The lower panels of Figure 5 present the maximum spatial correlations between the optimal modes (day 0 to day 20) and the day 0 composite height anomalies for each cluster, as a function of optimization time τ (in days). Correlations are computed over the clustering domain and weighted by the amplification factors of the top 10 optimal modes (amplification factors decrease sharply as in Figure S1 and become negligible beyond mode 10). To ensure the robustness of the analysis, the results in Figure 5 represent averages across the optimal modes derived from different linear damping and hyperdiffusion parameter sets (supporting Text S1).

The correlation analysis reveals an intriguing signal. The summer mean flow during the later period (2003-2023) produces lower correlations with Clusters 1 and 3 and higher correlations with Cluster 2. This behavior is remarkably consistent with the observed changes in cluster frequencies (Figure 2). This result remains consistent for all τ values, parameter choices, and clusters (Figures S2-S4). The robustness of the correlation trends indicates that the shifts in cluster occurrence frequency are largely driven by changes in the summer mean flow. In other words, evolving seasonal mean flows, related to either natural variability or anthropogenic forcing, modify the atmospheric instability properties (wave excitation) and the pathways of wave propagation, thereby altering the frequency of intense precipitation in the two monsoon fringe regions of interest.

4 Conclusions

This study investigates the large-scale circulation patterns responsible for intense summer (JJA) precipitation in two Asian monsoon fringes, i.e., Northeast China and Pakistan, where rainfall variability carries major socioeconomic impacts. By combining clustering of observations with idealized modeling, we identify the key flow regimes linked to regional intense precipitation events and assess how changes in the Northern Hemisphere summer background flow influence the relative occurrence frequencies of these flow regimes.

We first apply hierarchical clustering to classify the dominant circulation patterns associated with high-precipitation events in Northeast China. These clusters capture distinct pathways of Rossby wave propagation across the northern extratropics. To explore the dynamical origins of these circulation patterns, we employ an idealized barotropic model to investigate atmospheric instability in the upper troposphere during boreal summer. The model is linearized around two climatological background states corresponding to JJA of two periods (1982-2002 and 2003-2023). Nonmodal instability analysis subsequently identifies the most rapidly amplifying disturbances (optimal modes) for selected optimization times representative of the growth timescales of low-frequency, quasi-stationary disturbances.

The results show that changes in the summer mean flow modify large-scale wave excitation and propagation in the Northern Hemisphere. In particular, the waveguide has intensified and extended farther westward into Europe in recent decades. Over Asia, the waveguide exhibits strengthening and extension within the Asian subtropical jet region and weakening on the northern and southern flanks of the jet, consistent with the increased frequency of wave propagation along the central pathway. Optimal modes obtained from the instability analysis for the later period (2003-2023) further support this finding, exhibiting higher similarities with circulation patterns representing the central pathway of wave propagation (Cluster 2), while their correlations with the circulation patterns characterized by the zonal and equatorward pathways of wave propagation (Clusters 1 and 3) decrease in the later period. These findings establish the direct connections between changes in atmospheric background state and variations in the excitation and propagation of Rossby waves on that background. In a simplest-possible model setting, the contrasting properties of optimal disturbances obtained for the two periods provide insights into the origins of regional precipitation changes over the Asian monsoon fringes emphasizing the impacts of extratropical dynamical processes. Future work will investigate the root causes of the summer background flow changes and examine their attributions to natural variability and anthropogenic forcing, contrasting tropical and extratropical influences.

Acknowledgments

This study is supported by the U.S. National Science Foundation (NSF) through Grant AGS-2032532 and by the U.S. National Oceanic and Atmospheric Administration (NOAA) through Grant NA22OAR4310606.

Conflict of Interests

The authors declare that they have no competing interests.

Data Availability Statement

The observational precipitation data are produced by the Climate Prediction Center and archived by the NOAA Physical Sciences Laboratory (https://psl.noaa.gov/data/gridded/data.cpc.globalprecip.html). The ERA5 reanalysis data are available on the Copernicus Climate Change Service Climate Data Store (https://cds.climate.copernicus.eu/datasets/reanalysis-era5-pressure-levels).

References

Branstator, G. (2002). Circumglobal Teleconnections, the Jet Stream Waveguide, and the North Atlantic Oscillation. *Journal of Climate*, *15*(14), 1893–1910. https://doi.org/10.1175/1520-0442(2002)015%253C1893:CTTJSW%253E2.0.CO;2

Branstator, G., & Teng, H. (2017). Tropospheric Waveguide Teleconnections and Their Seasonality. *Journal of the Atmospheric Sciences*, *74*(5), 1513–1532. https://doi.org/10.1175/JAS-D-16-0305.1

Chen, F., Xu, Q., Chen, J., Birks, H. J. B., Liu, J., Zhang, S., et al. (2015). East Asian summer monsoon precipitation variability since the last deglaciation. *Scientific Reports*, *5*(1), 11186. https://doi.org/10.1038/srep11186

Dengri, A., & Yamada, T. J. (2024). Pakistan Floods in 2010 and 2022: The Impact of Extratropical Factors on Monsoon Systems. *Sola*, *20*, 281–290. https://doi.org/10.2151/sola.2024-037

Di Capua, G., Sparrow, S., Kornhuber, K., Rousi, E., Osprey, S., Wallom, D., et al. (2021). Drivers behind the summer 2010 wave train leading to Russian heatwave and Pakistan flooding. *Npj Climate and Atmospheric Science*, *4*(1), 55. https://doi.org/10.1038/s41612-021-00211-9

Ding, Y., Liang, P., Liu, Y., & Zhang, Y. (2020). Multiscale Variability of Meiyu and Its Prediction: A New Review. *Journal of Geophysical Research: Atmospheres*, *125*(7), e2019JD031496. https://doi.org/10.1029/2019JD031496

Gao, T., Wang, H. J., & Zhou, T. (2017). Changes of extreme precipitation and nonlinear influence of climate variables over monsoon region in China. *Atmospheric Research*, *197*, 379–389. https://doi.org/10.1016/j.atmosres.2017.07.017

Hersbach, H., Bell, B., Berrisford, P., Hirahara, S., Horányi, A., Muñoz-Sabater, J., et al. (2020). The ERA5 global reanalysis. *Quarterly Journal of the Royal Meteorological Society*, *146*(730), 1999–2049. https://doi.org/10.1002/qj.3803

Holton, J. R., & Hakim, G. J. (2013). *An Introduction to Dynamic Meteorology*. Academic Press.

Hoskins, B. J., & Ambrizzi, T. (1993). Rossby Wave Propagation on a Realistic Longitudinally Varying Flow. *Journal of the Atmospheric Sciences*, *50*(12), 1661–1671. https://doi.org/10.1175/1520-0469(1993)050%253C1661:RWPOAR%253E2.0.CO;2

Houze, R. A., Rasmussen, K. L., Medina, S., Brodzik, S. R., & Romatschke, U. (2011). Anomalous Atmospheric Events Leading to the Summer 2010 Floods in Pakistan. *Bulletin of the American Meteorological Society*, *92*(3), 291–298.

Hu, Y., Deng, Y., Lin, Y., Zhou, Z., Cui, C., & Dong, X. (2021). Dynamics of the spatiotemporal morphology of Mei-yu fronts: an initial survey. *Climate Dynamics*, *56*(9), 2715–2728. https://doi.org/10.1007/s00382-020-05619-2

Hurley, J. V., & Boos, W. R. (2015). A global climatology of monsoon low-pressure systems. *Quarterly Journal of the Royal Meteorological Society*, *141*(689), 1049–1064. https://doi.org/10.1002/qj.2447

Khan, S., & Hasan, M.-U.-. (2019). Climate Classification of Pakistan: Climate Classification of Pakistan. *International Journal of Economic and Environmental Geology*, *10*(2), 60–71. https://doi.org/10.46660/ijeeg.v10i2.333

Lau, W. K. M., & Kim, K.-M. (2012). The 2010 Pakistan Flood and Russian Heat Wave: Teleconnection of Hydrometeorological Extremes. https://doi.org/10.1175/JHM-D-11-016.1

Mak, M. (2011). *Atmospheric Dynamics*. Cambridge University Press.

Nanditha, J. S., Kushwaha, A. P., Singh, R., Malik, I., Solanki, H., Chuphal, D. S., et al. (2023). The Pakistan Flood of August 2022: Causes and Implications. *Earth's Future*, *11*(3), e2022EF003230. https://doi.org/10.1029/2022EF003230

Sardeshmukh, P. D., & Hoskins, B. J. (1988). The Generation of Global Rotational Flow by Steady Idealized Tropical Divergence. *Journal of the Atmospheric Sciences*, *45*(7), 1228–1251. https://doi.org/10.1175/1520-0469(1988)045%253C1228:TGOGRF%253E2.0.CO;2

Shen, B., Lin, Z., Lu, R., & Lian, Y. (2011). Circulation anomalies associated with interannual variation of early- and late-summer precipitation in Northeast China. *Science China Earth Sciences*, *54*(7), 1095–1104. https://doi.org/10.1007/s11430-011-4173-6

Simmons, A. J., Wallace, J. M., & Branstator, G. W. (1983). Barotropic Wave Propagation and Instability, and Atmospheric Teleconnection Patterns. *Journal of the Atmospheric Sciences*, *40*(6), 1363–1392. https://doi.org/10.1175/1520-0469(1983)040%253C1363:BWPAIA%253E2.0.CO;2

Sun, JianQi, & Ao, J. (2013). Changes in precipitation and extreme precipitation in a warming environment in China. *Chinese Science Bulletin*, *58*(12), 1395–1401. https://doi.org/10.1007/s11434-012-5542-z

Sun, Jianqi, & Wang, H. (2012). Changes of the connection between the summer North Atlantic Oscillation and the East Asian summer rainfall. *Journal of Geophysical Research: Atmospheres*, *117*(D8). https://doi.org/10.1029/2012JD017482

Sun, L., Shen, B., Gao, Z., Sui, B., Bai, L., Wang, S.-H., et al. (2007). The impacts of moisture transport of East Asian monsoon on summer precipitation in Northeast China. *Advances in Atmospheric Sciences*, *24*(4), 606–618. https://doi.org/10.1007/s00376-007-0606-8

Sun, L., Shen, B., Sui, B., & Huang, B. (2017). The influences of East Asian Monsoon on summer precipitation in Northeast China. *Climate Dynamics*, *48*(5), 1647–1659. https://doi.org/10.1007/s00382-016-3165-9

Tang, J., Xie, Y., Wu, Y., & Liu, G. (2023). Influence of precipitation change and topography characteristics on the development of farmland gully in the black soil region of northeast China. *CATENA*, *224*, 106999. https://doi.org/10.1016/j.catena.2023.106999

Trenberth, K. E., & Fasullo, J. T. (2012). Climate extremes and climate change: The Russian heat wave and other climate extremes of 2010. *Journal of Geophysical Research: Atmospheres*, *117*(D17). https://doi.org/10.1029/2012JD018020

Ullah, W., Karim, A., Ullah, S., Rehman, A.-U., Bibi, T., Wang, G., et al. (2023). An increasing trend in daily monsoon precipitation extreme indices over Pakistan and its relationship with atmospheric circulations. *Frontiers in Environmental Science*, *11*. https://doi.org/10.3389/fenvs.2023.1228817

Wang, B. (2006). *The Asian Monsoon*. Springer Science & Business Media.

Wang, Z., Yang, S., Lau, N.-C., & Duan, A. (2018). Teleconnection between Summer NAO and East China Rainfall Variations: A Bridge Effect of the Tibetan Plateau. https://doi.org/10.1175/JCLI-D-17-0413.1

Ward, J. H. (1963). Hierarchical Grouping to Optimize an Objective Function. *Journal of the American Statistical Association*, *58*(301), 236–244. https://doi.org/10.1080/01621459.1963.10500845

Webster, P. J., Magaña, V. O., Palmer, T. N., Shukla, J., Tomas, R. A., Yanai, M., & Yasunari, T. (1998). Monsoons: Processes, predictability, and the prospects for prediction. *Journal of*

Geophysical Research: Oceans, *103*(C7), 14451–14510. https://doi.org/10.1029/97JC02719

Xie, P., Chen, M., Yang, S., Yatagai, A., Hayasaka, T., Fukushima, Y., & Liu, C. (2007). A Gauge-Based Analysis of Daily Precipitation over East Asia. *Journal of Hydrometeorology*, *8*(3), 607–626. https://doi.org/10.1175/JHM583.1

You, Y., & Ting, M. (2021). Low Pressure Systems and Extreme Precipitation in Southeast and East Asian Monsoon Regions. *Journal of Climate*, *34*(3), 1147–1162. https://doi.org/10.1175/JCLI-D-20-0206.1

You, Y., Ting, M., & Biasutti, M. (2024). Climate warming contributes to the record-shattering 2022 Pakistan rainfall. *Npj Climate and Atmospheric Science*, *7*(1), 89. https://doi.org/10.1038/s41612-024-00630-4

You, Z., & Deng, Y. (2022). A Hierarchical Dissection of Multiscale Forcing on the Springtime Mesoscale Convective Systems in the United States. *Journal of Climate*, *36*(1), 39–54. https://doi.org/10.1175/JCLI-D-22-0150.1

You, Z., & Deng, Y. (2025). A Linear Analysis of the Heating Footprints of the U.S. Mesoscale Convective Systems in the Northern Extratropical Synoptic Variability. https://doi.org/10.1175/JCLI-D-24-0543.1

You, Z., Deng, Y., Ming, Y., & Dong, W. (2024). A multiscale assessment of the springtime U.S. mesoscale convective systems in the NOAA GFDL AM4. *Climate Dynamics*, *62*(5), 4017–4030. https://doi.org/10.1007/s00382-024-07114-4

Yu, X., & Ma, Y. (2022). Spatial and Temporal Analysis of Extreme Climate Events over Northeast China. *Atmosphere*, *13*(8), 1197. https://doi.org/10.3390/atmos13081197

Zhao, S., & Deng, Y. (2020). Nonmodal growth of atmospheric disturbances relevant to the East Asian pressure surge in boreal winter. *Climate Dynamics*, *54*(5), 3077–3089. https://doi.org/10.1007/s00382-020-05157-x

Zhao, S., Deng, Y., & Black, R. X. (2018). An Intraseasonal Mode of Atmospheric Variability Relevant to the U.S. Hydroclimate in Boreal Summer: Dynamic Origin and East Asia Connection. *Journal of Climate*, *31*(24), 9855–9868. https://doi.org/10.1175/JCLI-D-18-0206.1

Zhao, S., Deng, Y., & Li, W. (2020). A Nonmodal Instability Perspective of the Declining Northern Midlatitude Synoptic Variability in Boreal Summer. *Journal of Climate*, *33*(3), 1177–1192. https://doi.org/10.1175/JCLI-D-18-0799.1

Geophysical Research Letters

Supporting Information for

More Frequent Intense Precipitation on the Asian Monsoon Fringes Driven by Evolving Extratropical Planetary-Scale Circulations

Zhenyu You[1*], Yi Deng[1], Yi Ming[2], and Jaeyoung Hwang[1]

1. School of Earth and Atmospheric Sciences, Georgia Institute of Technology, Atlanta, GA, USA
2. Schiller Institute for Integrated Science and Society, Department of Earth and Environmental Sciences, Boston College, Chestnut Hill, MA, USA

**Corresponding author*: Zhenyu You (zhenyu.you@bc.edu)

Contents:

Text S1. Setup for the linear barotropic model

In this study, the barotropic model is applied at the 250 hPa pressure level on a midlatitude channel domain spanning 20°-80°N. The unforced quasi-geostrophic (QG) barotropic vorticity equation is written as (Holton & Hakim, 2013; Mak, 2011):

$$\frac{\partial \zeta}{\partial t} + f^{-1}J(Z, \zeta + f) = -\epsilon_1 \zeta - \epsilon_2 \nabla^4 \zeta \quad (1)$$

Here, the Jacobian operator $J(A, B) = A_x B_y - A_y B_x$ represents the horizontal advection terms. Vorticity ζ and geopotential Z are related to each other by the equation $\zeta = f^{-1} \nabla^2 Z$ in the QG system. $f = 2\Omega sin\varphi$ is the Coriolis parameter with Ω being the angular velocity of the Earth's self-rotation and φ is the latitude. Linear damping on relative vorticity is applied using a coefficient ε_1 to mimic the spin-down effect associated with the presence of a planetary boundary layer (Holton & Hakim, 2013). To improve model performance, differential damping is used over land and ocean. A hyperdiffusion term is added for scale selection to damp small-scale waves. The model is linearized around a background flow. In this study, two background flows are used: the JJA mean geopotential height at 250 hPa averaged over 1982-2002 and 2003-2023.

To test robustness, we select three combinations of linear damping parameters and three hyperdiffusion parameters:

Linear damping:

a. (40 days) $^{-1}$ over ocean and (20 days) $^{-1}$ over land
b. (20 days) $^{-1}$ over ocean and (10 days) $^{-1}$ over land
c. (10 days) $^{-1}$ over ocean and (5 days) $^{-1}$ over land

Hyperdiffusion: (0.8, 1.6, 3.2) × 10^{16} m ^{2} s $^{-1}$

The linear damping values reflect realistic timescales of large-scale atmospheric circulation decay at 250 hPa. The hyperdiffusion values are chosen within a range that damps grid- and subgrid-scale waves while preserving planetary-scale disturbances (Sardeshmukh & Hoskins, 1988; Simmons et al., 1983).

Text S2. Procedures for obtaining the optimal modes

First, we solve for the normal modes of the linearized barotropic vorticity model under a prescribed background state. After applying appropriate boundary conditions and discretizing the model using finite differences, the system can be expressed as follows:

$$\frac{dZ'}{dt} = AZ' \tag{2}$$

Here, *Z'* is a vector of length *N*, where *N* is the number of grid points in the model horizontal domain. **A** is the linear dynamical operator, a square matrix of size $N \times N$. Matrix **A** is the model's linear dynamical operator which contains all the information about this dynamical system such as the pre-determined parameters and the prescribed background state.

Assuming wave solutions, we write the prognostic variable *Z'* as:

$$Z'(\lambda, \varphi, t) = \Phi(\lambda, \varphi)e^{\sigma t} \tag{3}$$

where $\Phi(\lambda, \varphi)$ is the perturbation amplitude at a given model grid point (latitude φ and longitude λ). σ is the complex frequency with the real part indicating growth rate of the perturbation amplitude and the imaginary part indicating the perturbation frequency.

Substituting Equation (3) into the linearized equations (2), we obtain an equation in matrix form:

$$\sigma\Phi^{\mathrm{T}} = \mathrm{A}\Phi^{\mathrm{T}} \tag{4}$$

Equation (4) is solved as an eigenvalue problem where σ is the eigenvalue and Φ^{T} is the corresponding eigenvector, yielding *N* pairs of eigenvalues and eigenvectors. Each pair corresponds to one normal mode of the linear dynamical model.

We then use the obtained normal modes as base functions to derive optimal modes ψ for a specified optimization time τ, which aims to identify an initial perturbation that intensifies the most over the time interval τ in the specified basic flow. The geopotential perturbation at $t = \tau$ can be expressed as:

$$\psi(\lambda, \phi, \tau) = \sum_{i=1}^{N} \Phi_i \, e^{\sigma_i \tau} a_i = P\Lambda a \tag{5}$$

Here, **P** is a $N \times N$ matrix whose columns are composed of normal modes Φ_i. **Λ** is a diagonal $N \times N$ matrix with diagonal elements $\{e^{\sigma_i \tau}\}$. **a** is a vector containing the projection coefficients $\{a_i\}$ of the initial perturbation onto the normal modes. Following Mak (2011), the intensity of a perturbation at $t = \tau$ is calculated as

$$\mathcal{A}(\tau) = \psi^H D \psi = a^H \Lambda^H P^H D P \Lambda a = a^H B(\tau) a \tag{6}$$

where $\boldsymbol{\psi}^H$ is the Hermitian transpose of $\boldsymbol{\psi}$. **D** is an identity matrix if Euclidean norm is used. This is the default setup for "global optimization" (i.e., optimization across the entire model domain) in which all grid points are considered to carry the same weights in measuring the perturbation intensity. If perturbation growth over a particular region (local optimization) is to be emphasized, the diagonal elements of **D** corresponding to this region can be kept as 1 while other diagonal elements are set to small values such as 0.01.

The amplification factor (the ratio between an optimal mode's amplitude at the end of the selected time interval and its initial amplitude) of a disturbance is defined as

$$\gamma = \frac{a^H B(\tau) a}{a^H B(0) a} \tag{7}$$

Equation (7) can be further reduced to a new eigenvalue problem:

$$\gamma B(0)\mathrm{a} = B(\tau)\mathrm{a} \tag{8}$$

This again leads to N pairs of eigenvalues γ and eigenvectors **a**, and thus N optimal modes for every specified optimization time τ. For a given τ, the optimal mode with the largest amplification factor γ is denoted as the first optimal mode. The remaining optimal modes are ranked by decreasing values of γ. From Equation (5), the spatial structure of each optimal mode (corresponding to one pair of γ and **a**) at time t follows as:

$$\psi(\lambda, \phi, t) = \sum_{\mathrm{i}=1}^{\mathrm{N}} \Phi_{\mathrm{i}} \; e^{\sigma_i t} \mathrm{a}_{\mathrm{i}} \tag{9}$$

The spatiotemporal evolution of optimal disturbances can therefore be easily obtained.

Geophysical Research Letters

Supporting Information for

More Frequent Intense Precipitation on the Asian Monsoon Fringes Driven by Evolving Extratropical Planetary-Scale Circulations

Zhenyu You[1*], Yi Deng[1], Yi Ming[2], and Jaeyoung Hwang[1]

1. School of Earth and Atmospheric Sciences, Georgia Institute of Technology, Atlanta, GA, USA
2. Schiller Institute for Integrated Science and Society, Department of Earth and Environmental Sciences, Boston College, Chestnut Hill, MA, USA

**Corresponding author*: Zhenyu You (zhenyu.you@bc.edu)

Contents:

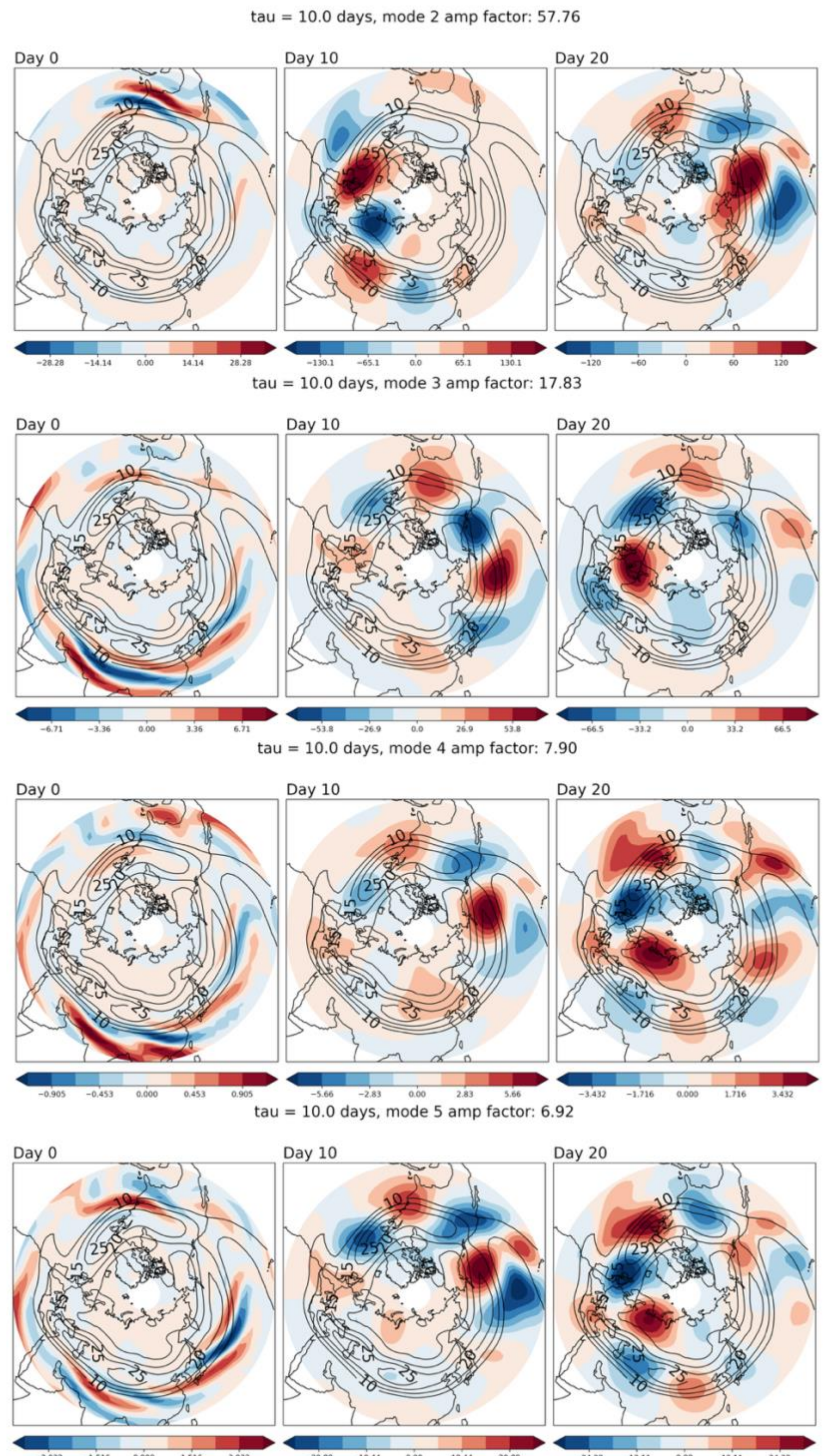

Figure S1. Evolution of optimal disturbances from the linear barotropic vorticity model for $\tau = 10$ days, showing modes 2-5. Each row presents one mode with its amplification factor indicated above the panels. Columns show the structures at day 0, day 10, and day 20. Shading represents geopotential anomalies, and contours indicate the climatological zonal wind (m s^{-1}).

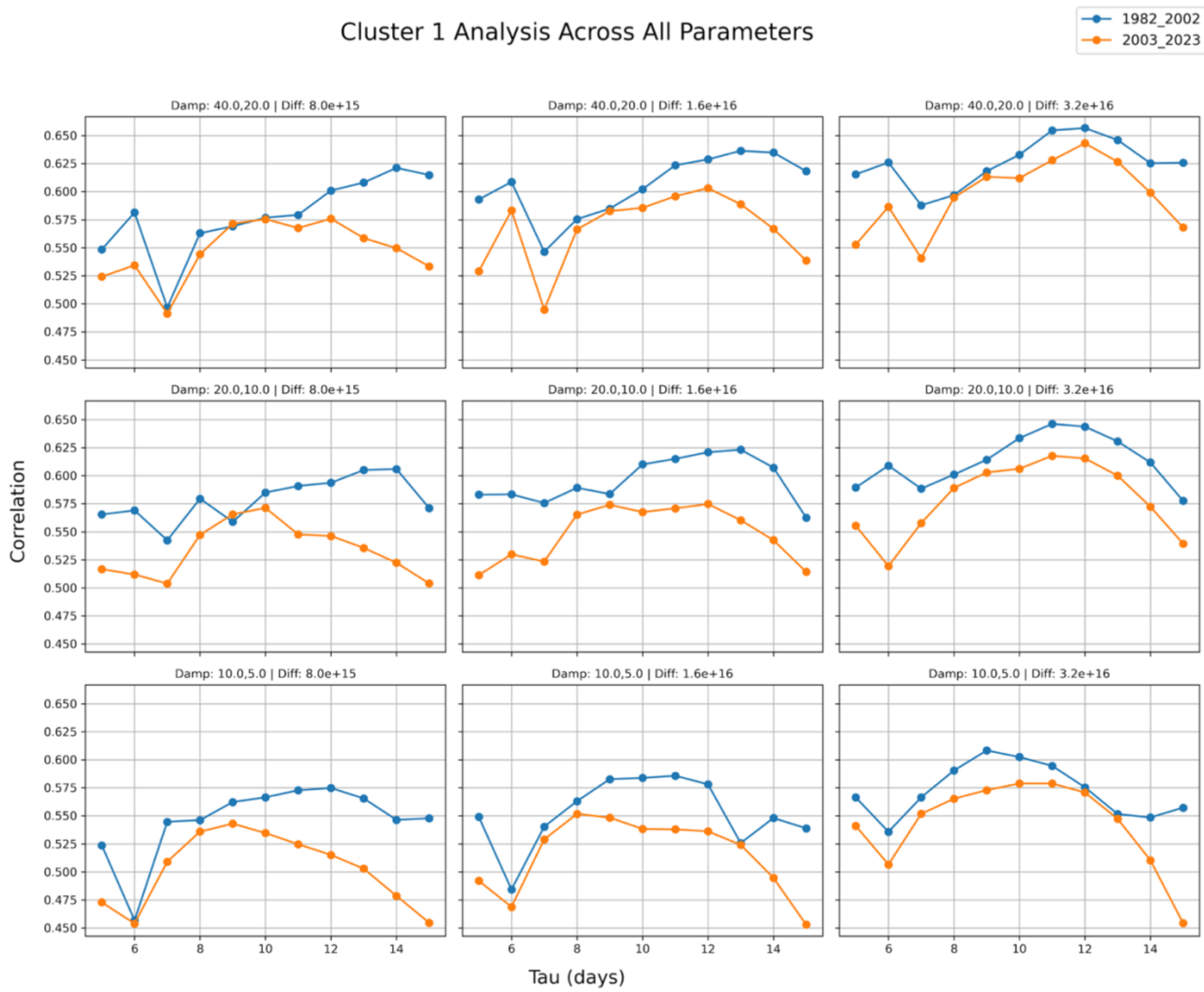

Figure S2 Correlations between optimal disturbances and the Cluster 1 composite pattern as a function of optimization time (τ, days). Rows show results for different linear damping values, and columns show results for different hyper-diffusion values. Blue lines represent the earlier mean flow (1982-2002), and orange lines represent the later mean flow (2003-2023). Each value is the average correlation of the top 10 optimal modes, weighted by their amplification factors.

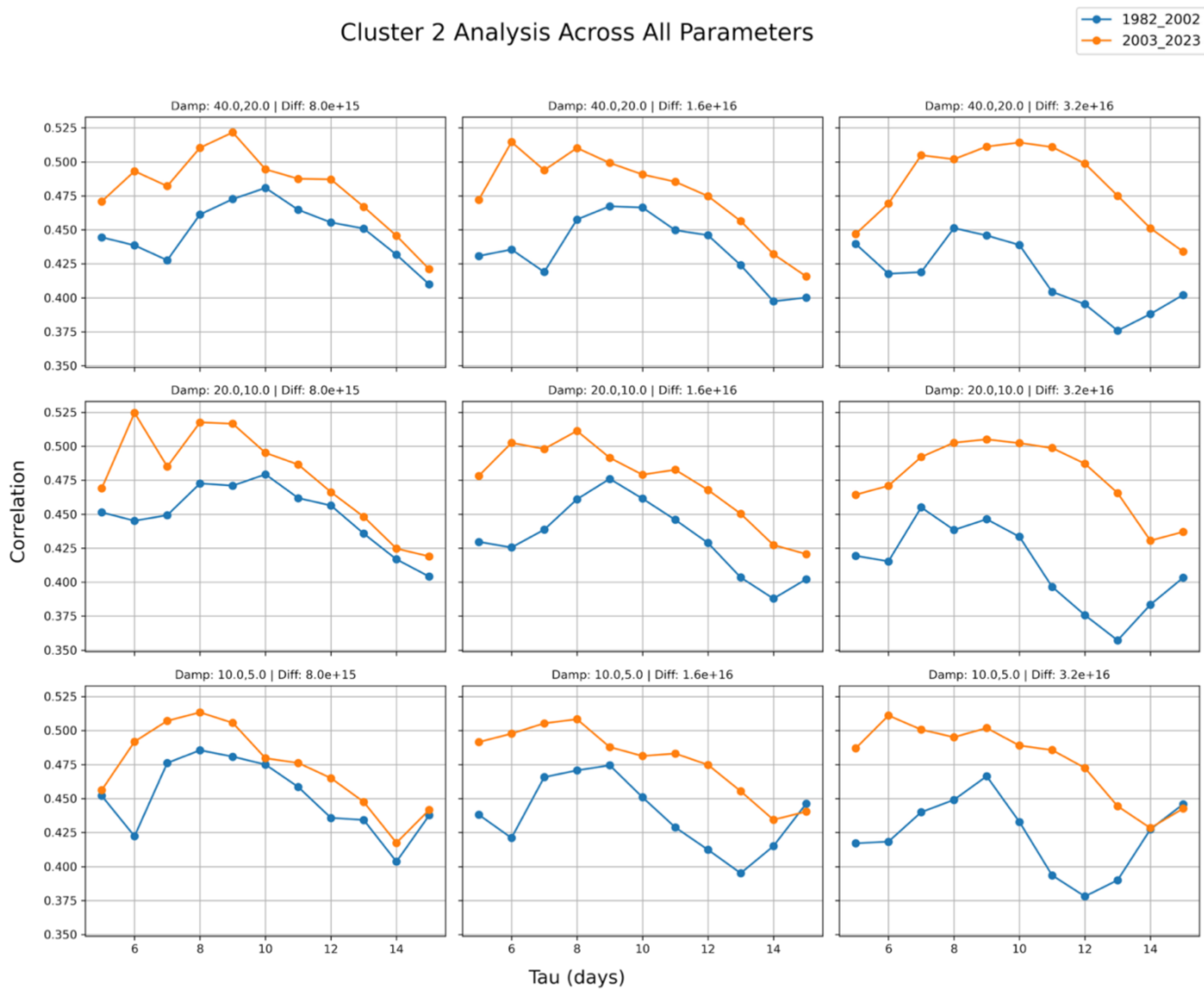

Figure S3. Same as Figure S2, but for Cluster 2.

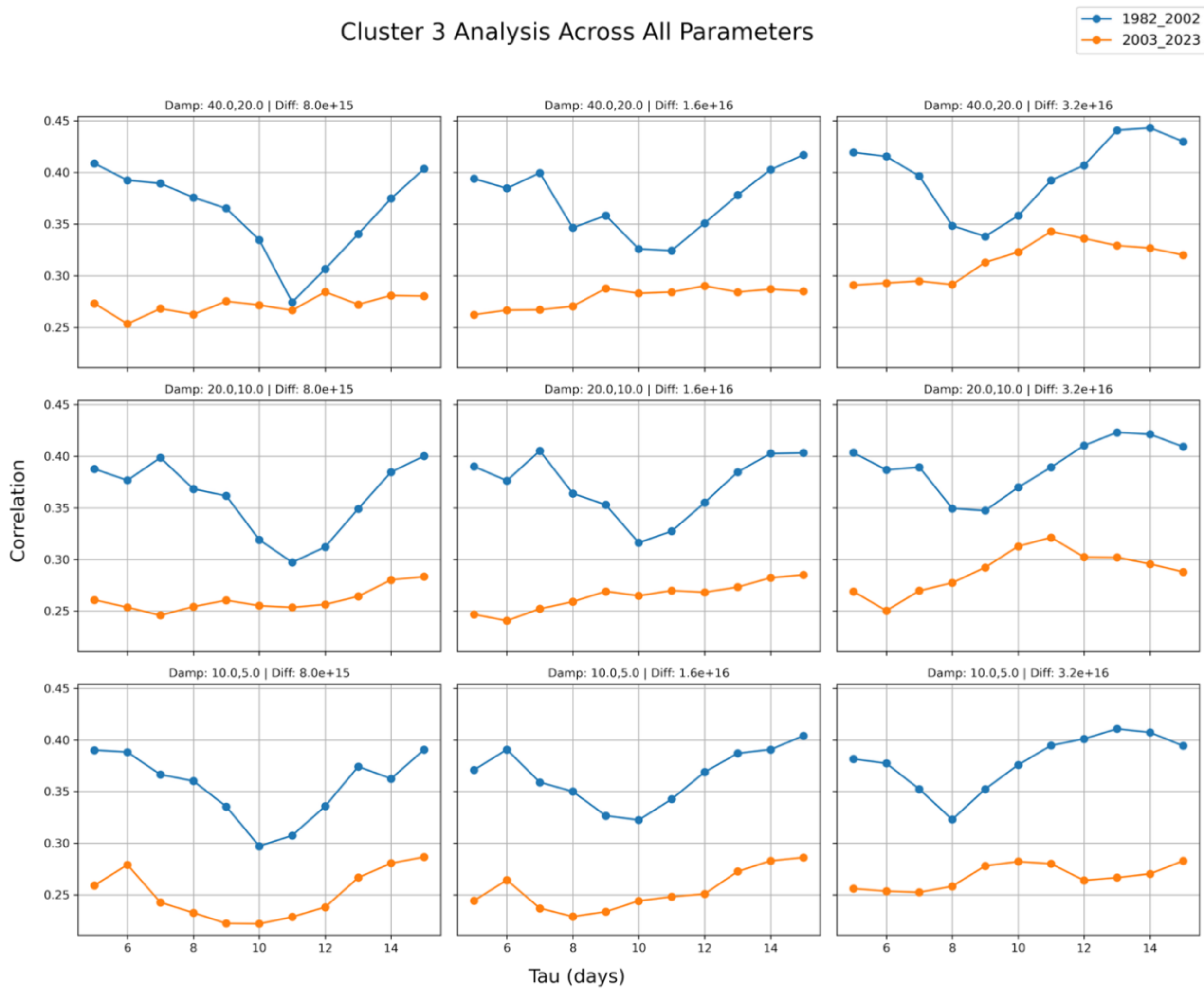

Figure S4. Same as Figure S3, but for Cluster 3.